Photoionization Dynamics in Pure Helium Droplets†

Darcy S. Peterka, Jeong Hyun Kim,‡ Chia C. Wang, Lionel Poisson,§ and Daniel M. Neumark*

Department of Chemistry, University of California, Berkeley, California 94720, and Chemical Sciences Division, Lawrence Berkeley National Laboratory, Berkeley, California 94720

Received: February 5, 2007; In Final Form: April 18, 2007

The photoionization and photoelectron spectroscopy of pure He droplets were investigated at photon energies between 24.6 eV (the ionization energy of He) and 28.0 eV. Time-of-flight mass spectra and photoelectron images were obtained at a series of molecular beam source temperatures and pressures to assess the effect of droplet size on the photoionization dynamics. At source temperatures below 16 K, where there is significant production of clusters with more than 10^4 atoms, the photoelectron images are dominated by fast electrons produced via direct ionization, with a small contribution from very slow electrons with kinetic energies below 1 meV arising from an indirect mechanism. The fast photoelectrons from the droplets have as much as 0.5 eV more kinetic energy than those from atomic He at the same photon energy. This result is interpreted and simulated within the context of a "dimer model", in which one assumes vertical ionization from two nearest-neighbor He atoms to the attractive region of the He_2^+ potential energy curve. Possible mechanisms for the slow electrons, which were also seen at energies below IE(He), are discussed, including vibrational autoionizaton of Rydberg states comprising an electron weakly bound to the surface of a large He_N^+ core.

1. Introduction

This paper presents a study of the photoionization of pure helium droplets above the ionization energy of atomic helium. It is motivated by a desire to understand the energetics and dynamics of ionization and electron escape in pure helium droplets and, by extension, the differences between ionization in pure and doped helium droplets. Photoelectron imaging and photoionization time-of-flight mass spectrometry are combined to examine ionization processes in helium droplets. The two measurements, taken over a wide range of droplet sizes, provide new insight into the complex ionization phenomena that occur within helium droplets.

There have been numerous investigations on the electron impact[1−8] and photoionization[9−12] of pure and doped helium droplets in which ion mass spectrometry was used as the detection method. An essential feature common to rare gas clusters, especially helium, is that the neutral species are only weakly bound, at long range, by van der Waals interactions, while the cationic systems are strongly bound by covalent interactions, and have greatly reduced equilibrium bond distances. As a result, the cation, when formed, is highly vibrationally excited, typically with >1 eV of internal energy. The relaxation of vibrational energy within the cluster leads to fragmentation. The presence or absence of any particular ion in the mass spectra is then related to many factors, but more often reflects the fragmentation dynamics of the cluster and the relative stability of daughter ions rather than the initial state of the cluster. The appearance energy of the fragment ions also does not necessarily correlate with either the adiabatic ionization energy or the vertical ionization energy of the nascent cluster. In helium droplets, both electron impact ionization and photoionization lead to extensive fragmentation of the cluster, with the resulting cluster ion distributions only weakly dependent on the initial droplet size.[4,9]

Though the mass spectra resulting from electron impact ionization and photoionization of droplets are similar, photoionization provides two significant advantages over electron impact: it deposits a well-defined amount of energy into the droplets, and it creates a photoelectron. In photoionization, the initial absorption takes place under the aegis of the Franck−Condon principle. If the ionization is direct and the electron escapes without strong subsequent interactions, the photoelectron spectrum explicitly contains information about the initial state of the neutral cluster and the nascent ion. If the ionization is indirect, the electron kinetic energy may be decoupled from the initial excitation and the electron energy and angular distributions modified, with both measurements sensitive to the interaction between the droplet atoms and the escaping electron.

Our group[13] previously used photoelectron imaging to examine the photoionization of pure helium droplets below the atomic helium ionization energy, IE(He) = 24.59 eV. We found that ionization was the result of an indirect autoionization process and that the emitted electrons had very little kinetic energy, typically <1 meV, for photon energies ranging from 23.0 to 24.5 eV. Although no definitive energy loss mechanism was assigned, it appeared that the emitted electron interacted strongly with the helium environment before escape. This result contrasted markedly with later experiments on doped helium droplets. Multiphoton ionization experiments by Radcliffe et al.[14] on silver clusters inside helium droplets showed fast photoelectrons, with little apparent modification to their kinetic energy. The only change attributable to the droplet environment was a slight asymmetry in the photoabsorption peaks, and what appeared to be a fast (sub-nanosecond) relaxation in the intermediate state. Loginov et al.[15] measured photoelectron

† Part of the "Roger E. Miller Memorial Issue".

* Corresponding author. E-mail: dneumark@berkeley.edu.

‡ Current Address: School of Chemical and Biological Engineering, College of Engineering, Seoul National University, Seoul 151−744, Korea.

§ Current address: Laboratoire Francis Perrin, CEA/DSM/DRECAM/SPAM-CNRS URA 2453, DSM CEA Saclay, 91191, Gif-sur-Yvette Cedex, France.

10.1021/jp0710032 CCC: $37.00
Published on Web 06/16/2007

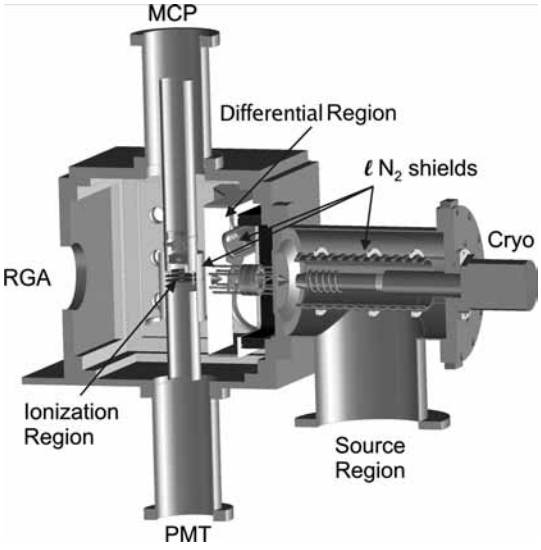

Figure 1. Schematic of the helium machine with main components indicated.

images from multiphoton ionization of aniline inside a helium droplet, finding photoelectrons that were both faster and slower than those seen from bare aniline. However, despite a broadening of the peaks in the photoelectron spectra, and some slow photoelectrons, most electrons appeared to escape without strong retardation from the cluster. The photoelectron kinetic energy was directly coupled to the incoming photon energy in both experiments—excess energy deposited in the excitation led to faster photoelectrons. In the multiphoton experiments, the energy of a single photon, and even of the multiple photons used for dopant ionization, is below that of any possible electronically excited state in the cluster. The droplet is completely transparent, and the ionization of the dopant is direct. Nevertheless, neither optical transparency of the droplet nor direct dopant ionization appears necessary for the emission of fast electrons: a similar result was seen in the single photon ionization of SF_6 inside helium droplets.[10] Here, the droplet absorbed the photon, and ionization was mediated by the droplet, yet the photoelectron spectra were relatively unperturbed from those of bare SF_6.

The above results on doped droplets have led us to reinvestigate pure droplets over a wider photon energy range, particularly above the ionization potential of atomic He, using photoelectron imaging. Above IE(He), the new experiments show fast, blue-shifted electrons attributed to direct ionization and very slow electrons, similar to those seen previously from indirect ionization.[13] The production of both types of electrons is strongly correlated with changes in the droplet size distribution, which aids in understanding the microscopic dynamics responsible for the disparate electron kinetic energies.

2. Experimental Section

The experiments were carried out on the Chemical Dynamics Beamline at the Advanced Light Source.[16] A schematic of the instrument is shown in Figure 1. Most of the experimental apparatus has been described in detail elsewhere.[10] A continuous He droplet beam was produced by expanding 60 bar of helium gas through a 5 μm aperture at source temperatures (T_s) from 11 to 50 K. This temperature range allowed us to access two different expansion regimes[17−20] and greatly vary the average cluster size: with subcritical expansion conditions the cluster size varied from 1 atom to 10^4 atoms, while under critical expansion conditions (below ~16 K at 60 bar, see below) much larger droplets are produced, from 10^4 to $>10^6$ atoms. The droplet beam then passed through a 1.5 mm skimmer and entered a differential region, which can also be used as a pickup region for doping the droplets.[10,11] After leaving the differential region through a 2 mm skimmer, the droplet beam entered the main chamber and was ionized with VUV synchrotron undulator radiation. The bandwidth of the VUV light used was ~35 meV and the flux was $\sim 10^{13}$ photons·s^{-1}.

Two different detector assemblies were used: one for photoions and one for photoelectrons. Ion time-of-flight mass spectrometry (TOF-MS) was performed using a 0.6 m Wiley−McLaren[21] time-of-flight mass spectrometer and a pair of 40 mm MCPs coupled to a conical anode. The ion counts were recorded using a multichannel scaler (Fast Comtec P7886, 500 ps time resolution). For the ion time-of-flight measurements, the pseudocontinuous synchrotron radiation was modulated by a patterned chopper wheel rotating at 600 Hz.[10] The resultant mass spectra had a resolution of $m/\Delta m > 400$ and could be collected at a repetition rate of 20 kHz. Photoelectron imaging was carried out using a standard velocity-mapped lens system[22] where the electrons were detected with a pair of 80 mm MCPs coupled to a phosphor screen, imaged with a 12 bit, 1 megapixel digital camera (DALSA 1M30), and integrated using a computer. The image is a two-dimensional projection of the three-dimensional nascent photoelectron distribution. Electron kinetic energy (eKE) and angular distributions were obtained from the images using standard methods.[23,24]

3. Results

Figure 2a shows time-of-flight mass spectra (TOF-MS) as a function of source temperature following 25 eV photoexcitation. For display purposes, the ordinate intensity is in units of $\sqrt{\text{counts}}$. In these spectra, peaks from the residual gas in the ionization chamber are seen (H_2O [18], N_2 [28], O_2 [32]) and will be ignored. The mass range recorded for most of the TOF-MS was 0−600 amu, but no resolvable signal was seen above ~400 amu. Measurements extending to 1600 amu showed no additional detectable He-dependent features. In all the spectra, mass 4, He^+, is the strongest signal. At source temperatures below 20 K, the next largest He-related signal is He_2^+, mass 8, which is then followed by a series of peaks of mass 4*n*, the He_n^+ cluster ions. The peak at mass 56, He_{14}^+, attributed to a complete solvation shell surrounding a He_2^+ ion core,[25] is stronger than the surrounding He_n^+ features. All of the helium droplet spectra show additional modal structure in the He_n^+ ion distributions, but this will not be discussed in detail (see Figure 2b). For all source temperatures below ~20 K, the integrated intensity of the He_n^+ peaks for $n \geq 2$, which can only come from helium clusters, is larger than that of the helium atom peak, and indicates clear contributions from the droplets in our experiment.

The relative intensities of the He_n^+ peaks change markedly with temperature. Initially, as the temperature is dropped, the intensity of all the He_n^+ ions increases, with the region between 16 and 18 K showing a maximal signal for nearly all of the He_n^+ peaks. With further decreases in temperature, the smaller He_n^+ peak intensities change very little, while the higher He_n^+ peaks drop rapidly. Measurements with a small quadrupole mass spectrometer (SRS RGA 200) show similar behavior. These trends were also seen in earlier measurements of Buchenau et al.[17] with electron impact ionization and could be inferred from the photoionization work of Fröchtenicht.[9] In our experiments, at source temperatures of 16 K, the ratio of counts of He_n^+, $n = 10-100$, to that of He_n^+, $n = 1, 2$, was a few times larger than at 13 K, as can be seen more clearly in the linear intensity

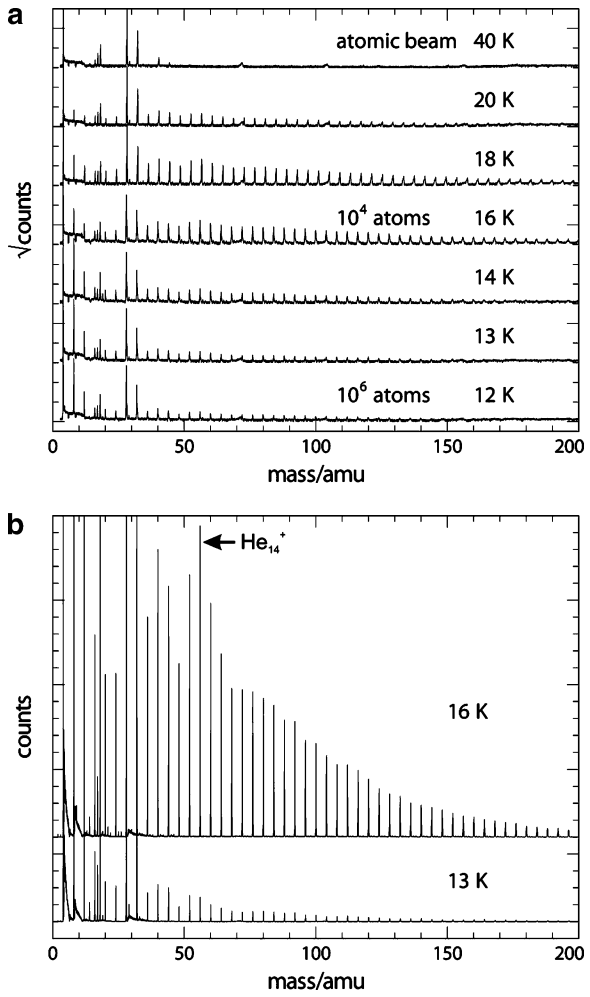

Figure 2. (a) TOF-MS illustrating trends for different source temperatures (average droplet sizes). The scale for the ordinate is in units of $\sqrt{\text{counts}}$. (b) Representative TOF-MS for droplets formed with source temperatures of 16 and 13 K following 25 eV photoexcitation.

plot in Figure 2b. Looking at a specific surrogate, the He_{14}^+: He_2^+ ratio was ~10 times larger at 16 K than at 13 K. The changes in ratios are mainly due to a sharp decrease in the larger He_n^+ ions, with minor contributions from changes in He^+ and He_2^+. The total recorded ion signal varied by at most a factor of 3 as a function of temperature between 12 and 20 K, and was maximal at temperatures between 16 and 18 K.

Figure 3 shows raw photoelectron images following 25.0 eV (25.02 actual energy) excitation as a function of source temperature. Images taken at other energies (from IE(He) = 24.59 to 28.0 eV) show similar features. In particular, there were no appreciable changes in the images or resultant photoelectron distributions near 25.7 eV, the energy required to create a free electron in bulk liquid helium.[26] (The conduction band of an electron in liquid helium is ~1 eV greater than that in vacuum because of the strong Pauli repulsion between the free electron and the $1s^2$ electrons on the helium atoms.[27]) In all of the images, the VUV radiation was linearly polarized, with the polarization axis matching the long axis of the figure.

The first image, taken at a nozzle temperature of >30 K, where no droplets are expected, shows the particularly pronounced simple structure expected from the ionization of atomic helium. The ground state neutral helium atom has an electron configuration of $1s^2$, and single photon ionization with linearly polarized light can only lead to pure p-wave emission. As a result, the image is strongly anisotropic, with no intensity at the equator. The atomic ion also has no available excited states at these photon energies, so the electron kinetic energy (eKE) distribution is nominally a delta function.

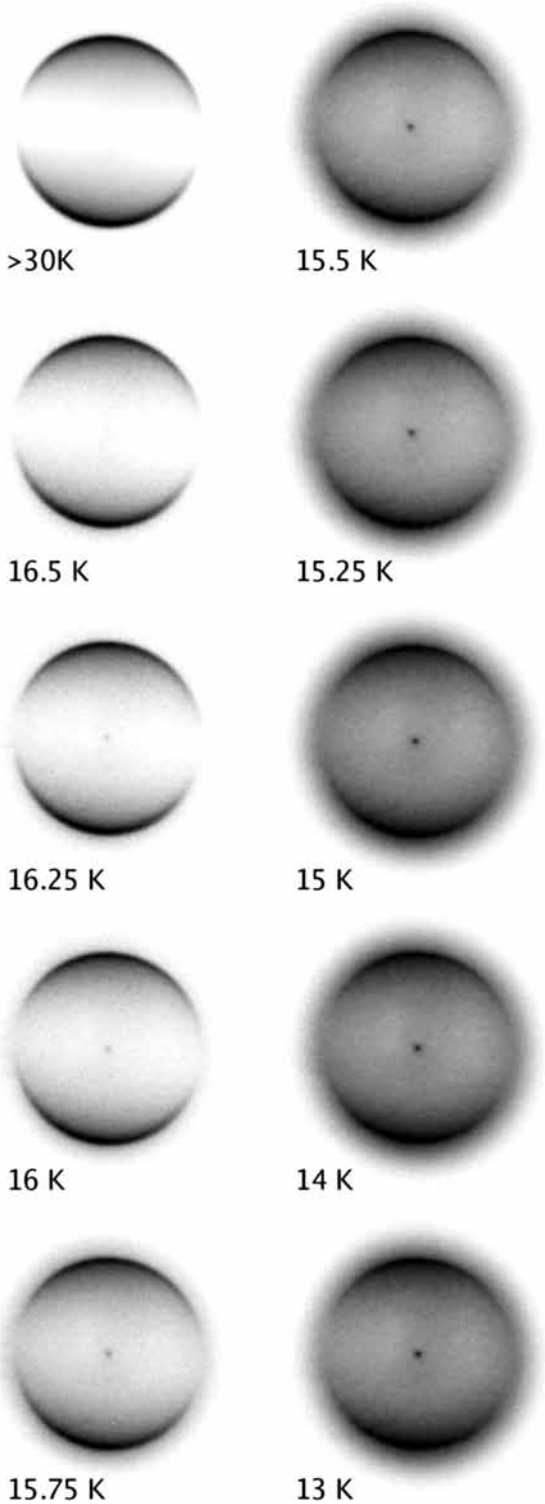

Figure 3. Photoelectron images of helium beam at 25.0 eV photon energy with indicated source temperatures. In all of the images the light is linearly polarized, and parallel to the long axis of the figure.

As the source temperature is lowered and helium clusters begin to be produced, there is little change in the images. Further decreases in temperature, to ~16.25 K, result in the first noticeable new features. A faint center feature can be seen, and the image begins to show intensity at the equator. Between 16 and 15.5 K, the images change markedly, with a prominent halo

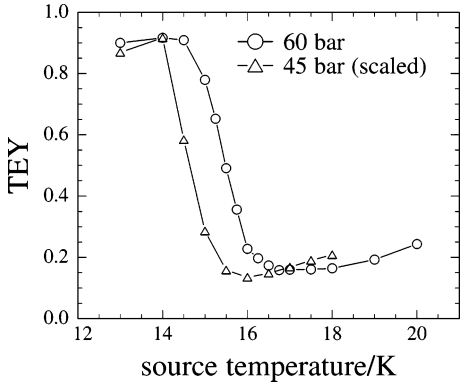

Figure 4. Total electron yield (TEY) as a function of source temperature.

appearing around the atomic signal, extending to larger radii. In regions where there previously was very little or no intensity, there are now photoelectrons. There is considerable broadening of the outer feature, and modifications are seen throughout. The presence of equatorial intensity reduces the overall anisotropy of the image. The faint center feature seen at 16 K grows in strength as well. With additional decreases in temperature, the new features become more pronounced (15−14 K) before seemingly stabilizing (14−13 K). Other images (not shown) taken with temperatures down to 11 K, the lowest stable temperature maintained by our source at 60 bar backing pressure, are nearly identical to those at 13 K.

For display purposes, the images in Figure 3 are scaled independently; a plot of the integrated intensities of the raw images (total electron yield [TEY]) is shown in Figure 4. The total signal decreases slowly as the temperature is dropped, followed by a steep rise beginning near 16 K and plateauing near 14 K. The average total intensity of images taken between 13 and 14 K is about 6 times greater than for those taken between 16 and 18 K. This is in stark contrast with the integrated TOF-MS, which showed much smaller changes in intensity between the warm (16−20 K) and cold (below 14 K) source conditions, and near maximal total signal between 18 and 16 K. Also shown in Figure 4 is the total integrated image intensity at ∼45 bar source pressure (scaled for display). It has the same behavior as the 60 bar data, but is shifted by ∼0.8 K toward lower temperatures.

The eKE distributions derived from the images in Figure 3 are shown in Figure 5a with zooms of the distributions shown in Figure 5b,c. The photon energy was 25.02 eV, so for atomic helium (the >30 K image) we expect a single feature, a sharp peak at ∼0.43 eV ($E_{h\nu}$ − IE(He)). The width of this peak, ∼50 meV fwhm, is a reflection of the bandwidth of the light (larger contribution) and blurring in the electron imaging system (smaller contribution). With decreasing temperatures, the peak initially broadens, and an asymmetrical shading appears on the sharp peak. Photoelectrons are now seen with both higher and lower energies than those from atomic helium. Though elements of these features can be seen at all droplet-forming temperatures, they grow strongly when the source temperature drops below 16 K. At the lowest temperature, the once sharp peak has a prominent shoulder toward higher eKE, and a smoother, weaker tail toward lower energy. As mentioned previously, images taken at different photon energies give distributions with similar shapes, but are offset by the change in excitation energy. The escaping electrons, and hence the ionization itself process, thus appear directly coupled to the photoexcitation. Looking closer at the energetics, the high-energy electrons extend to ∼0.9 eV, about 0.5 eV beyond those from atomic helium. From the shape

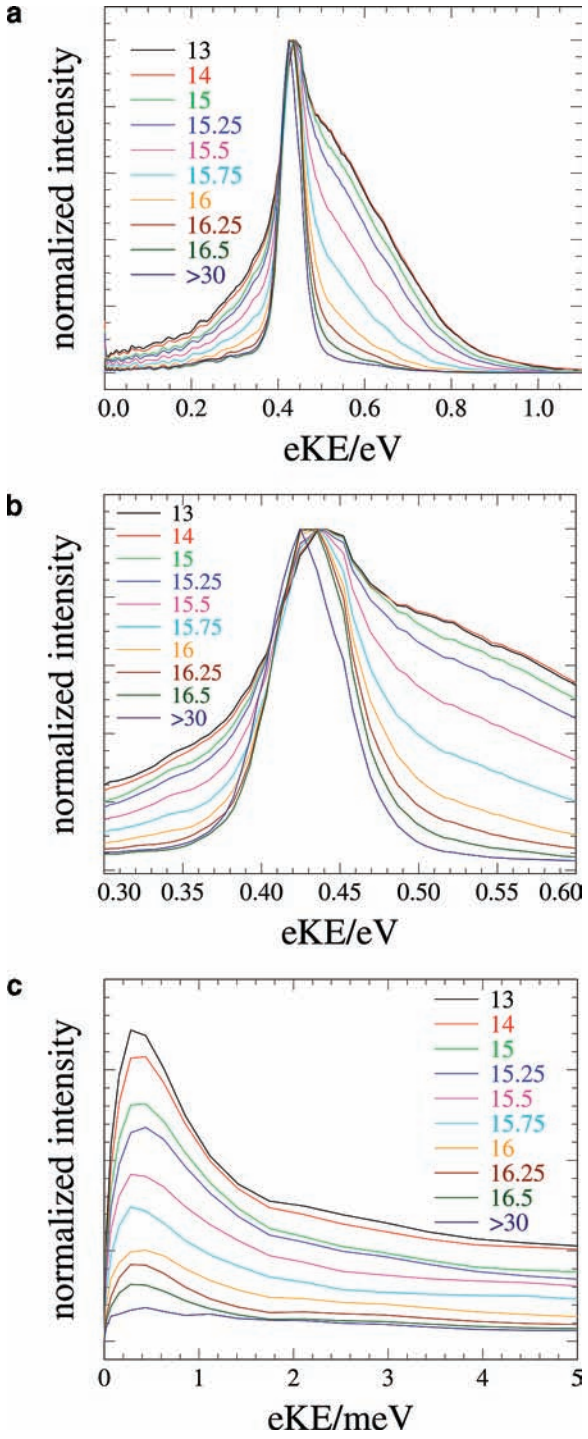

Figure 5. Photoelectron kinetic energy distributions following 25.0 eV photoionization of helium beam with indicated source temperatures. (a) Entire distribution; (b) area near the peak; (c) lowest kinetic energy electrons.

of the shoulder, it appears the "peak" of the shoulder is shifted ∼70 meV toward faster photoelectrons when compared with the atomic peak. From the total intensity measurements, the images, and the eKE distributions, we can estimate the cluster contribution by subtracting an appropriately scaled atomic image from the cluster images; with this procedure, the contribution to the total photoelectron image that is "clusterlike" in nature is less than 20% of the total signal at 17.5 K, 50% at 16 K, and more than 90% at 14 K.

Focusing on the very low energy portion of the eKE distributions, shown in Figure 5c, we see a sharp peak that grows

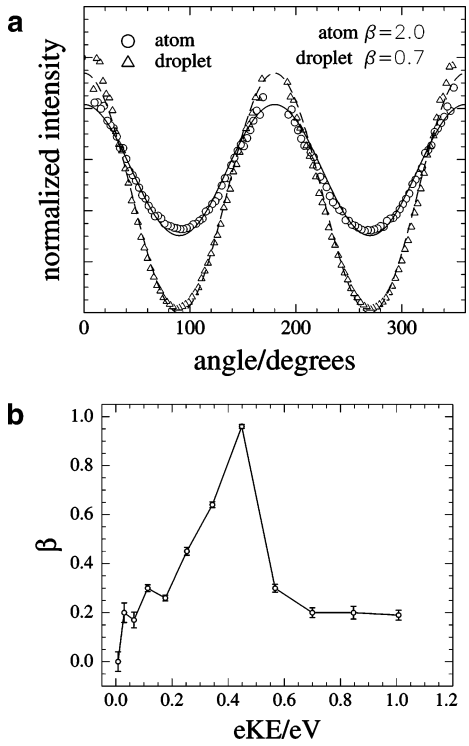

Figure 6. (a) Angular distributions derived from the 14 K image (△) and the >30 K image (○). Panel b shows the anisotropy parameter β as a function of electron kinetic energy for the 14 K droplet image.

with decreasing source temperatures, similar to what was seen for helium droplets below IE(He).[13] This electron signal peaks at very low kinetic energy (<1 meV), and the width of this peak is significantly smaller than the bandwidth of the VUV radiation. This feature does not shift in energy with changes in the photon energy, and appears decoupled from the optical excitation process. Its temperature dependence is similar to, but not identical with, that of the total image. The intensity rise of this feature appears to be offset ~0.25 K toward higher temperatures, and the ratio of "center intensity" to total intensity increases as the temperature is lowered, indicating that this feature is growing faster than the total intensity (we somewhat arbitrarily define the center feature as electrons with eKE < 5 meV, and will call these electrons "slow" in distinction from the electrons with energies near 0.4 eV, which we call "fast"). However, at 12 K, the center feature still represents less than 2% of the total integrated photoelectron signal at 25 eV.

Below IE(He), the slow electron feature represents a much larger fraction of the total electron yield, about 20% at 23.8 eV.[13] This result largely reflects the absence of the fast peak from direct ionization at this photon energy. However, the total integrated intensity of the slow peak also depends on the photon energy. At 14.5 K, the intensity of this feature, as determined by integrating the signal with eKE ≤ 5 meV, is about a factor of 2 higher at 23.8 eV than at 25 eV. At energies between these values, the low-energy signal has an additional contribution from near-zero-energy electrons produced by direct ionization near IE(He). Above 25 eV, the slow peak declines gradually but never disappears entirely.

The angular distributions derived from the atomic helium image and the 14 K image are shown in Figure 6. The upper panel shows the distributions for the entire image. Fitting the distributions using the familiar expression for anisotropy,[28] $I(\theta) = \{(1/4)\pi\}\{1 + \beta P_2(\cos\theta)\}$, yields $\beta = 2.0$ for the atomic beam, as is expected. Photoelectrons for $T_s = 14$ K have less anisotropy, with the overall image giving $\beta = 0.7$. However, while the atomic image is described by a single anisotropy parameter, the droplet images are not; the electron angular and kinetic energy distributions are coupled. Figure 6b shows the anisotropy parameter as a function of electron kinetic energy for the 14 K image. In the droplet image, the overall intensity and anisotropy are highest at electron kinetic energies corresponding to that of the atomic helium signal, but the maximal value for the anisotropy is significantly lower, $\beta = 1.0$. As one goes to either higher or lower energy photoelectrons, the images become less anisotropic, with the slowest electrons being essentially isotropic.

4. Discussion

The photoelectron images and resultant spectra of the pure droplets show two distinct channels of electron emission. The major channel is the emission of "fast" electrons that are seen with kinetic energies up to 0.5 eV greater than those expected from the ionization of atomic helium. These fast electrons have energies that are directly coupled to the incoming photon energy. The minor channel is the emission of isotropic, very low kinetic energy electrons, for which the eKE distribution has no apparent dependence on the incoming photon energy. The vastly different kinetic energies, angular distributions, and dependence on excitation energy of the two electron channels lead us to postulate distinct microscopic dynamics for their production. Yet, interestingly, the intensities of both channels, as well as the total electron yield, are strongly coupled to changes in the source temperature, with a similar dependence, indicating a common factor between the two. It is with this temperature dependence that we will start the discussion.

A. Temperature Dependence of the Intensity. In the He expansion leading to droplet formation, three regimes are possible: subcritical, critical, and supercritical. Extensive time-of-flight studies have identified some of the temperatures and pressures where the transition between regimes occurs.[17,19,29,30] Using them as a guide for our experiment, we first note that our machine is incapable of generating the very large droplets (>10^9 atoms) in the supercritical regime,[20] because our source cannot reach the requisite temperatures at 60 bar helium backing pressure (~10 K). In most experiments on helium droplets, the helium droplets are created by condensation in a subcritical expansion (regime I).[1,17,18] In this regime, the droplet size distribution is log-normal; thus a significant number of droplets are well below the mean size. Also present is a substantial atomic helium signal from the initial expansion. Under these conditions, the size dependence of the cluster beam as a function of temperature and pressure is well-known;[18,19] our droplets consist of ~1×10^3 atoms at 22 K and ~$(1-2) \times 10^4$ atoms at 16 K.

At lower source temperatures, the isentropes pass near the helium critical point (regime II).[17] While many interesting effects occur under these source conditions,[17,29,31] the three most important for our experiment are that the atomic helium component of the beam appears to decrease, the average droplet size increases sharply, and the overall flux increases dramatically.[17,20,29] Examining the pressure−temperature phase diagram for helium,[17] we estimate that, with 60 bar backing pressure, the transition to the critical regime should begin near 16 K, precisely where we observe the marked transition in the total electron yield (Figure 4) and the strong changes in the photoelectron spectra (Figure 5). The offset in temperature for the 45 bar data shown in Figure 4 is also consistent with our predictions for the onset of regime II. The large increase in helium flux as the temperature is lowered[17,29] matches the overall changes in the total integrated electron yield.

Previous experiments[17,29,30] have shown that during the transition from regime I to regime II, the cluster size distribution bifurcates, split between the original subcritical size distribution and a new distribution with significantly larger droplets and an exponential form.[32] With continuing decreases in source temperature, the intensity of the original distribution decreases, with concomitant gains in the intensity of the larger droplet distribution, for which the average droplet size ranges from 10^5 to 10^7 atoms.[20] We believe that this repartitioning of the overall helium flux into significantly larger droplets results in the strong modifications observed in the photoelectron distributions. The two-component distribution is also consistent with the actual appearance of the photoelectron spectra, where the fast component grows to become a well-defined shoulder on the original peak, with an abrupt change in slope between the two at the coldest temperatures (see Figure 5).

A bifurcated droplet size distribution also explains the apparent discrepancy between the intensities in the TOF-MS in Figure 2, in which the ion fragments associated with droplets appear to decrease while the integrated photoelectron signal increases below 16 K. Specifically, while our photoelectron imaging system efficiently collects all photoelectrons, the TOF-MS collection efficiency drops off sharply at masses above ~1600 amu owing to the perpendicular extraction geometry. Fröchtenicht et al.[9] performed retarding field measurements of the cluster ion fragments following photoionization and showed that, under similar source conditions, the fragmentation process resulted in cluster ions with $N^+ > 5 \times 10^3$ atoms. As we cannot effectively detect ions of this size, there is a disparity between the electron imaging and ion time-of-flight measurements. As the droplet size gets larger, and the total photoelectron intensity gets higher, the He^+ and He_2^+ signal remains nearly constant, and the smaller cluster ions ($N < 100$) decrease strongly. Thus all the additional electrons below 16 K result from ionization of large droplets. In such droplets, the ratio of interior to surface atoms is much higher than for droplets generated in subcritical expansions, so the increased photoelectron yield can be attributed specifically to ionization of interior atoms.

Note that in our previous study[13] of pure He droplets below IP(He) we reported the average droplet size as $N \approx 10^4$. However, in light of the results discussed above, we carefully reevaluated the experimental conditions and temperature dependences of the slow photoelectrons seen in that work and believe the expansion conditions under which slow electron signal was optimal corresponded to regime II, with an average droplet size considerably larger than 10^4.

B. Mechanism of Fast Electron Production. Our experiments show that the photoionization of large helium droplets gives rise to electrons with kinetic energies greater than those of the atom. In direct photoemission, the electron's expected kinetic energy can be easily determined from the Einstein relation: eKE = $h\nu$ − IE. For photoionization with 25 eV photons, the expected eKE for electrons from atomic helium is 0.43 eV (25.02 − 24.59 eV); for the droplets we detect electrons with energies over 0.9 eV, ~0.5 eV greater than the atomic photoelectrons.

In a recent photoelectron imaging study on the multiphoton ionization of aniline within helium droplets, Loginov et al.[15] detected electrons with kinetic energies as much as 0.12 eV greater than those from bare aniline, and successfully interpreted the shift in the aniline ionization energy with a simple model. The surrounding helium atoms were treated as a homogeneous dielectric medium, and the IE shift was a result of instantaneous relaxation of the dielectric during ionization. The expected lowering of the ionization energy of a moiety inside the droplet compared to the bare species is then given by the following equation:[33−35]

$$\Delta_{IE}(R) = -\frac{z^2q^2}{8\pi\epsilon_0}\left(1-\frac{1}{\epsilon_e}\right)\left(\frac{1}{r_0}-\frac{1}{R}\right) \quad (1)$$

where r_0 is the effective radius of the spherical hole containing the positive charge, ϵ_e is the effective dielectric constant of the material, and R is the droplet radius.

We can estimate the spherical hole by $r_0 = [\int\{g(r)/r^2\}\,dr]^{-1}$, the form suggested for liquids,[36] with $g(r)$ being the radial distribution function for helium,[37] and find $r_0 = 2.4$ Å. Using the known low-temperature dielectric constant of liquid helium,[38,39] eq 1 gives $\Delta E_{IE} \approx -0.16$ eV, the polarization energy of a nascent positive hole in liquid helium,[2] which is significantly smaller than our observed shift. If we attempt to fit the much larger shifts seen in our experiment with eq 1, the value of r_0 required is $r_0 = 0.8$ Å. While there is some uncertainty in defining r_0,[36] this value is unreasonably small by any standard, given that the average He−He distance in liquid He is 3.6 Å. Hence, the polarization continuum model is insufficient to explain the fast photoelectrons seen from large pure helium droplets.

This result is not particularly surprising, since there are profound differences between the system studied by Loginov et al.[15] and our system. In the doped system, the ionization energy of the dopant is much lower than that of helium. As a result, the dopant ion−helium interaction is dominated by polarization forces, and there are no strong covalent contributions. In contrast, in the pure helium system, the $He-He^+$ interaction is very strong, and is dominated by covalent interactions. The simplest molecular cation, He_2^+, for instance, is bound by over 2 eV,[40,41] and could easily account for the greatly lowered vertical ionization energy compared to polarization forces alone. Covalent interactions have been shown to influence the overall energetics of all of the ionic rare gas cluster systems,[42] and have indeed been implicated in the photoelectron spectra of other rare gas clusters. Peel and co-workers[34,43] have examined He Iα photoelectron spectra from pure rare gas clusters (Xe, Kr, and Ar) and found that the shape of the spectra could not be interpreted from a polarization model alone. In their experiments, Franck−Condon simulations proved to be an invaluable tool in the interpretation and understanding of their photoelectron spectra, and clearly showed the involvement of molecular ion cores.

Based on these considerations, we will attempt to interpret our photoelectron spectra within the context of a Franck−Condon (FC) picture in which vertical ionization accesses the attractive region of a cationic He_n^+ core, resulting in faster photoelectrons than in atomic He. We will use the simplest possible molecular core, He_2^+. In helium, the overall energetics of the neutral and cationic dimer systems are well-known.[40,44,45] For any internuclear separation of two helium atoms, the energy required for ionization is simply given by $V(r)_{He_2^+} - V(r)_{He_2}$. The positional distribution of the atoms, which governs the region of Franck−Condon overlap between the curves, determines the overall appearance of the obtained spectra. Our implementation of this picture is described in the following section.

(i) Nearest-Neighbor Distributions and Photoelectron Simulation. In the usual FC simulations of photoelectron spectra, the geometries of the lower and upper states are fixed, and the nature of the spectrum is determined by displacements along the

appropriate normal coordinates. Since He droplets are liquid, a somewhat different approach is needed. For both bulk liquid helium and helium droplets, the radial distribution function $g(r)$ is known,[37] and this gives positional information about the atoms in the droplet. If we pick an arbitrary helium atom in the cluster, there will be many other helium atoms nearby, with a distribution of distances, and the average He−He distance is ∼3.6 Å. If we simply compute the energy of ionization for a helium pair with an internuclear spacing of the average helium−helium distance, the lowering in ionization energy is negligible, on the order of 10^{-4} eV, and clearly cannot explain our recorded spectra. However, for the purposes of evaluating the observed photoelectron spectra, the *average* distance is not the most important. He_2^+ is a strongly bound, covalent system, and the energetics are extremely sensitive to internuclear distance. In the first solvation shell, *one* of the helium atoms is closest, and it is likely that it is this atom that will play a dominant role in affecting the energetics. For the remainder of this paper, we will call this one helium the *nearest neighbor*, using this strict definition. As the helium droplet is liquid, there is a distribution of distances for this nearest neighbor, and we will denote this distribution $nn(r)$.

The radial distribution function, $g(r)$, is clearly dependent on the nearest-neighbor distribution, but the entire nearest-neighbor distribution cannot be easily extracted from $g(r)$, as $g(r)$ is an average of *all* the atoms. We do expect $nn(r)$ to match $g(r)$ on the leading edge, with the shortest distances, as the nearest neighbor will be the dominant contributor, but we need more information. To determine $nn(r)$, we performed path integral quantum Monte Carlo (PIMC) calculations using the Universal Path Integral framework.[46,47] Our initial calculations for small ($N < 120$) clusters showed that, with increasing cluster size, both $g(r)$ and $nn(r)$ become more sharply peaked toward smaller r. For $g(r)$, calculations by Krotscheck and Chin show that this trend clearly continues, with the large droplets' radial distributions quickly converging toward that of the bulk.[37] The largest clusters in our experiment comprised on the order of 10^6 atoms, and it was not computationally feasible to perform an exact calculation. Instead, to simulate the largest clusters, the calculations were done with ∼100 helium atoms in a box, with periodic boundary conditions (S3 topology). The density was chosen to match the experimentally determined average density for the helium droplets near this size,[18] but calculations with slightly different densities showed no substantive quantitative differences in $nn(r)$. In using periodic boundary conditions and the average density, we are neglecting the surface of the cluster in our simulation. At the surface of the droplet, there is a variation in density, with experiments indicating a surface thickness of 6−7 Å (90−10% density). The neglect of these atoms in our simulation does not change $nn(r)$ significantly. First, at droplet sizes of $\sim 10^4$ atoms, the surface atoms make up less than 20% of the total atoms in the droplet; at 10^5 atoms, the surface atoms consist of less than 10% of the total atoms. Second, because the helium density drops near the surface, the atoms are more widely spaced and they will contribute only to the tail of the $nn(r)$ distribution. Helium pairs, at these longer internuclear distances, interact very weakly and the system is more "atomic" in nature; as a result, these atoms are unlikely to be responsible for the production of the fastest photoelectrons. Figure 7a shows a portion of the radial distribution function, $g(r)$, and the nearest-neighbor distribution, $nn(r)$, that result from our calculations.

Comparing $nn(r)$ to $g(r)$, we see that the maximum in $nn(r)$ occurs at significantly shorter internuclear separation, ∼3.05 Å, than $g(r)$, ∼ 3.60 Å. As expected, the leading edge of $g(r)$ matches $nn(r)$. The nominal shortest helium−helium separation is ∼2.1 Å, which is still far greater than the He_2^+ equilibrium distance, 1.08 Å,[40,41] but is less than or equal to the average internuclear spacing of vibrational states $v^+ \geq 17$. Because of the relatively high vibrational state, and the potential of inhomogeneous broadening from the surrounding heliums, we treat the possible initial and final states as continua. With $nn(r)$, we can now complete our Franck−Condon simulation by weighting $E_{h\nu} - [E_{He_2^+}(r) - E_{He_2}(r)]$ by $nn(r)$, and generate a photoelectron spectrum. Figure 7b shows a schematic of the process. The intensity of the resulting spectrum was scaled to fit the fast portion of the observed spectra ($0.48 < eKE < 1.1$ eV), using a nonlinear-least-squares method, but is otherwise unmodified. The comparisons of some representative fits to the experimental data are shown in Figure 8. The dependence of the fit scaling coefficients on temperature matches the temperature dependence of the total integrated image intensity, indicating that the fast photoelectron component is largely responsible for the enhanced integrated signal and strongly correlated with the production of large droplets. The match between the observed spectra and the simulation is good, and although the theoretical work of Gianturco et al.[41,48] clearly shows that the presence of even a third helium complicates the ionic potential energy landscape, the dimer model does quite well in both the shape of the distribution and the overall energetics, and should be considered the dominant factor in the dynamics of ionization.

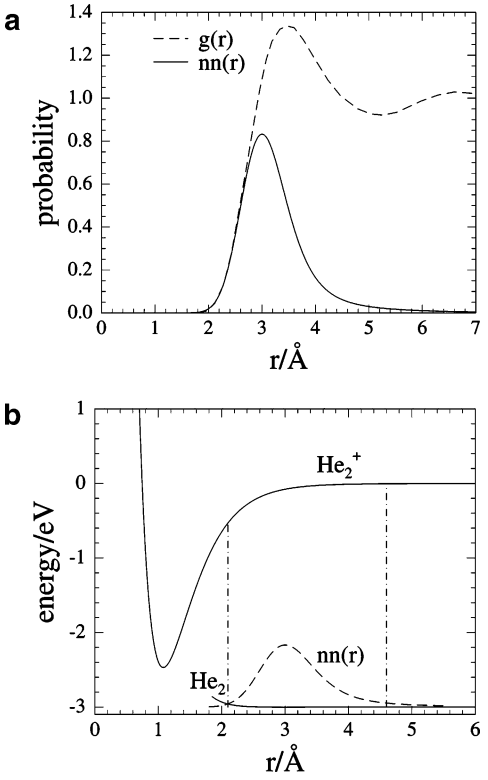

Figure 7. (a) Computed radial distribution function, $g(r)$, and nearest-neighbor distribution, $nn(r)$, for a helium droplet (see text for details). (b) Relevant curves for the Franck−Condon simulation of the fast electron signal. The zero of energy is relative to $He + He^+$. The He_2 curve has been shifted up ∼21.6 eV to make it visible on this plot.

(ii) General Considerations. Our results show that, at photon energies above IE(He), the photoelectron spectra are dominated by fast electrons whose energy spectrum can be approximated by a simple FC picture, indicating that direct ionization is the primary process of interest. Hence, these fast photoelectrons apparently pass through the droplet and escape without signifi-

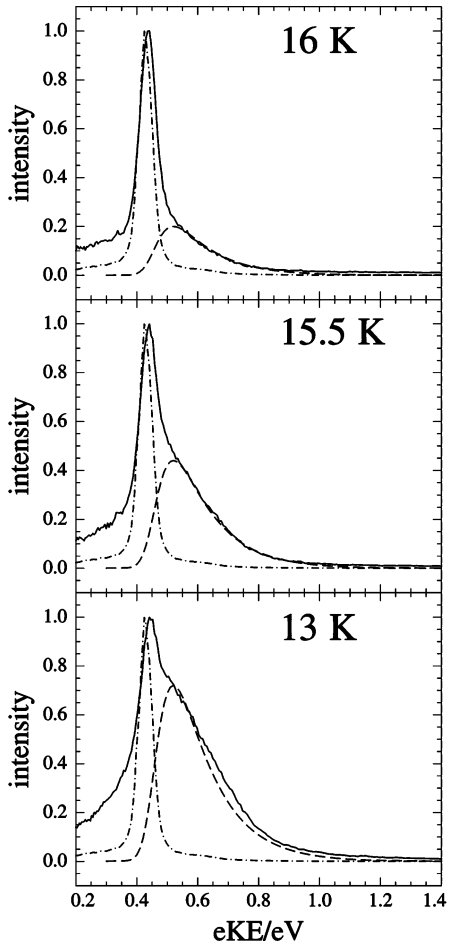

Figure 8. Comparisons of the Franck−Condon simulation to the observed spectra for indicated source temperatures. In the plots, the solid line shows the observed droplet spectrum, the dashed line shows the FC simulated fast component, and the dot−dashed line shows the atomic helium spectrum. The simulated spectrum is scaled by fitting it to the fast component (0.48 < eKE < 1.1 eV) of the observed spectra, but is otherwise unmodified.

cant slowing. We noticed no obvious change in the either the overall intensity or the photoelectron distribution as we scanned the excitation energy from IE(He) to a few eV above the conduction band (1.1 eV above the vacuum level) in liquid helium. These results are of interest given that electrons injected into in bulk liquid He at energies >1.1 eV rapidly localize to form a "bubble" state, in which the electron is "thermalized" with the surrounding He atoms.[27,49−52] The bubble radius is 17 Å, and the ground state of the electron within the bubble lies about 0.1 eV above the vacuum level. The fast photoelectrons are clearly escaping the droplet without becoming trapped in a bubble, regardless of whether the photon energy lies below or above the bulk conduction band.

This result is of interest in light of studies by Möller and co-workers[53] of the fluorescence excitation spectrum of He droplets. Although this spectrum shows a large drop at IE(He), it clearly extends beyond IE(He). Here, the signal decays gradually, to near zero by 25.7 eV, i.e., at the expected onset of the conduction band in He droplets. They suggested that fluorescence above IE(He) arises from recombination of a trapped electron with the positive hole created by ionization, and that the cutoff above 25.7 eV is from injection of the electron into the conduction band and its subsequent escape from the droplet, eliminating the possibility of recombination. Our results, however, show that electron production by direct ionization is the dominant electron emission process in all energy regimes above IE(He), regardless of whether bubble formation or fluorescence are available as parallel channels.

Our observation of fast electrons below the conduction band likely reflects the finite size of our droplets. Before localization, the electron must first slow enough to be trapped in the corrugated potential of the helium droplet.[27] In a femtosecond multiphoton ionization study on bulk liquid helium, Benderskii et al.[54] saw evidence of bubble formation and were able to predict and measure the nominal distance the electron traveled, all the while undergoing near-elastic collisions, before it localized, and found it to be on the order of 100 nm. Our electrons have lower initial kinetic energies, but applying similar arguments, we estimate the average distance the electrons would travel before beginning to localize is >40 nm, which is larger than the nominal radius of our largest droplets. Note that the fast photoelectrons do show possible evidence for inelastic electron−helium scattering, namely the tail toward lower eKE (relative to atomic helium photoelectrons) and, possibly, the reduction of anisotropy in the helium droplet photoelectrons compared with the atomic photoelectrons (see Figure 6). Similar interactions have been noted in experiments on doped droplets.[10,15]

C. Slow Electrons in Helium Droplets. In this section, we consider the properties and mechanistic origins of the very slow electrons responsible for the sharp central spots in the images in Figure 3. In contrast to the fast electrons, which bear the hallmarks of direct photoionization, the electron kinetic energy distribution of the slow electrons is independent of photon energy. The shapes of these distributions at 25 eV in Figure 5c are very similar to those obtained previously at 23.8 eV (where no direct ionization was seen), and no significant changes are seen at photon energies up to 27 eV. This decoupling of the kinetic energy distribution from the photon energy implies that the slow electrons arise from an indirect ionization mechanism involving significant electron−He interactions. In addition, the temperature dependence of the slow electrons shows that they are strongly correlated with droplet size and, like the fast electrons, become prominent when the expansion conditions for the helium change from subcritical to critical. Combined with the changes in the time-of-flight mass spectra, and hence the fragment cluster-ion mass distribution, the appearance of the slow electrons is clearly correlated with production of the largest helium droplets.

In our earlier work below IE(He),[13] we proposed that the slow photoelectrons resulted from a complex, indirect mechanism involving (a) excitation of a Rydberg state of He_2* within the droplet that autoionizes to form He_2^+ or a larger cationic core, and (b) "thermalization" of the resulting electron via electron−He interactions prior to its leaving the droplet. The importance of Rydberg-like excitations in He droplets below IE(He) has been established in the fluorescence excitation spectra by Möller and co-workers,[53,55] and the role of molecular autoionizing states was first suggested by Fröchtenicht et al.[9] to explain the onset of photoionization below IE(He). The idea of electron thermalization was motivated by the observation that much of the eKE distribution below IE(He) could be fit using the functional form for thermionic emission from a very cold cluster (T < 6 K).

We first consider whether the excitation process leading to slow electrons differs above and below IE(He). As discussed in Section 3, the slow electron signal just above IE(He) at 25 eV is about a factor of 2 less than at 23.8 eV. The significance of this drop is not entirely clear, although we note that a similar drop is seen in the fluorescence excitation spectrum[53] of He droplets. It is possible, for example, that the Rydberg autoionization mechanism proposed below IE(He) is no longer operative

by 25 eV, and that the slow electron signal results instead from the small fraction of electrons produced by direct ionization of He atoms that is unable to escape easily from the droplet, in contrast to the vast majority of electrons that leave relatively unperturbed. Regardless of how these electrons are initially formed, there must be significant electron−He interactions for them to be so slow. The rest of the discussion is focused on the nature of these interactions, expanding on some of the concepts outlined in our earlier work.

Collisions between electrons and He atoms are an inefficient means for electrons to lose energy, owing to the large mass ratio between the collision partners. Electron thermalization is greatly facilitated if the excess electron is trapped by the droplet for any length of time. Possible mechanisms for this trapping are suggested by previous experimental and theoretical work on electrons in bulk He and in negatively charged droplets. In the bulk, electrons can reside either inside the liquid, in a bubble state,[27,50,56−59] or on the liquid helium surface, bound by the electron's image potential.[60−62] Experimental studies of the temperature dependence of the mobility of electrons inside liquid helium have shown that the electron bubble encounters a small barrier, ∼40 K, near the liquid−vapor interface that hinders the electron's escape.[63] The stability of a bubble state near the liquid helium interface has been studied in a series of density functional calculations by Ancilotto and Toigo.[64,65] They calculated a barrier to escape of ∼38 K, in good agreement with experiments.[63] The bubble was found to be "mechanically unstable" with respect to rupturing, with subsequent escape of the electron, at surfaces distances of less than 23 Å. The instability is partly caused by the change in density at the surface; the surface tension of the spherical bubble cavity depends strongly on the density ($\propto\rho^4$), and the decrease in density near the surface leads to a decrease in the total energy of the system as the electron is ejected.

In studies of electron attachment to neutral helium clusters, yielding a negatively charged droplet, it was found that the minimum size required for stable electron capture was $N = 7.5 \times 10^4$; no signal was seen from smaller clusters.[32,66] A helium droplet with an excess electron can, in principle, support both surface and interior electron states.[27,32,58,61,67−69] However, lifetime measurements by the groups of Northby and Toennies seemed to preclude surface states:[66,70] the calculated binding energy of an excess electron to the surface of even a very large helium droplet was too weak. Calculations by Rosenblit and Jortner also predicted that the first bound surface state would require a droplet with $N > 3.0 \times 10^5$[5,61,67] larger than the minimum size detected in experiments. The electrons were thus postulated to be in the bubble states, and subsequent measurements of the difference in detachment of electrons from droplets of ^{3}He and ^{4}He appeared to confirm the electron's location as inside the droplet.[71] The minimum droplet size seen supporting the bubble state, $N = 7.5 \times 10^4$, is still significantly larger than the minimum size cluster, $N \approx 5 \times 10^3$, predicted theoretically to support an electron bubble in the absence of dynamic effects (tunneling escape, etc.).[72]

In our experiment, production of a photoelectron is accompanied by cation production, leading to a rather different physical situation than in a negatively charged droplet. Thus, for example, if an electron bubble were formed, it would have a nonnegligible interaction with the cationic cluster core, resulting in an exciton-like state whose properties have thus far not been considered theoretically. The slow photoelectrons could result from the bubble "bursting" when it approaches the surface of the droplet, similar to the process studied theoretically at the surface of bulk liquid He by Ancilotto and Toigo.[64,65] The observation that slow electrons occur only from large droplets is consistent with bubble formation; in smaller droplets, electrons can more easily escape without being trapped. One problem with the bubble picture is that there is a barrier at the surface of the droplet with respect to electron escape, and such a barrier might be expected to result in an electron kinetic energy distribution peaking further away from zero than is seen experimentally. On the other hand, the presence of the positive charge may significantly reduce the barrier height or mitigate its effects.

Surface-bound states may be considerably more favored in our experiments than for negatively charged droplets. Calculations by Sekatskii[73] predicted the existence of novel Rydberg states for neutral He droplets bigger than ∼40 Å in diameter ($N \geq 7 \times 10^2$), with the electron bound outside the droplet to the positively charged ion core. The induced dipole interaction between the cation and the surrounding heliums favors a centrally located ion core, and the conduction band of the droplet limits the tunnel penetration depth of the electron wave function into the droplet to <3.4 Å, effectively preventing the electron, which is trapped by the Coulomb potential, from recombining with the ion core. The possible existence of these states leads to an intriguing alternate mechanism for slow electron production, namely vibrational autoionization involving conversion of the very low frequency internal modes of the cationic core into electronic energy.

The internal energy needed for vibrational autoionization could easily result from the disruptive effects associated with formation of the positive ion core. In most systems, and certainly in pure helium droplets, the interaction between the initial ion and the surrounding helium atoms is much stronger than the neutral interactions. This leads to rearrangement and droplet restructuring around the ion core, and evolves heat. For doped droplets, numerous studies demonstrate effective heat transfer to the droplet, with experiments on doped helium droplets showing rapid cooling of the nascent ions.[4,10,74,75] In pure helium droplet systems, He_2^+ is either formed directly, or very quickly, and has significant vibrational energy (∼2 eV). Theoretical predictions indicate that vibrational relaxation is very fast, and should be comparable to the formation time of an electron bubble.[27,76,77] The energy released in this process will heat the cluster and can result in ejection of the weakly bound Rydberg electron, analogous to thermionic emission seen in much hotter clusters.[78−80]

The idea of slow electrons arising from autoionizing surface states has considerable appeal, but must be considered in light of other effects. First, there is the issue of how surface states would be formed via photoexcitation. The correlation of the slow electron signal with large droplets suggests that it results from excitation of interior He atoms, not surface atoms. Since the outer electron has very little overlap with the droplet interior, these states cannot be accessed from direct excitation of the cluster, but instead rely on some means of transporting the electron from the interior to the surface of the cluster. In this sense, the "bubble" and "surface" pictures are not mutually exclusive. Electrons with high kinetic energies can simply escape the Coulomb potential, so it may be that initial bubble formation is needed to effectively transport an electron to the surface of the cluster, where it can couple to a surface-bound Rydberg state (recall that the electron wave function for the surface state penetrates ∼3 Å into the droplet[73]).

A second point of interest is that the energy realized upon formation of a cationic core can not only eject an electron, but

also result in substantial fragmentation of the droplet, as evidenced by the fact that He_2^+ is the dominant ion seen from either electron impact or photoionization under most conditions. Evaporation of He atoms could very well occur on the same time scale transport of the bubble to the droplet surface, an effect that could place additional constraints on the minimum droplet size for slow electron production. If the original droplet is too small, then even if a bubble is formed, the positively charged core remaining after evaporation may not be large enough to support a surface Rydberg state that is stable with respect to recombination, consistent with our observation that slow electrons are only seen from large droplets.

5. Conclusion

Our measurements represent the first energy-resolved photoelectron spectra from pure helium droplets above the atomic ionization threshold, and show the power of photoelectron imaging in elucidating ionization and relaxation processes in pure helium droplets. Additional information comes from comparison of the photoelectron yields with time-of-flight mass spectra of the photoionization products. The results indicate that while the smaller droplets formed in subcritical expansions yield photoelectrons with nearly "atomic" distributions, the larger droplets formed in critical expansions give fast electrons, with energies significantly higher than those that can be explained by polarization interactions alone, and implicate covalent participation from molecular cores. The fast electrons appear to arise from direct ionization to molecular cations, and we were able to fit our spectra with a Franck−Condon simulation based on He_2 that considered the nearest-neighbor helium distribution. Although the actual ionization process probably involves more than two helium atoms,[41,48] reasonable quantitative agreement with the experimental spectra can be achieved considering only pairs of He atoms. This simulation technique should not be unique to pure helium droplets, but should hold for any dopant whose positive ion has strong covalent interactions with the helium environment.

Although the photoelectron images under critical expansion conditions are dominated by fast photoelectrons, they also exhibit a weak, slow component peaking at eKE < 1 meV, and the kinetic energy distribution of this component is largely independent of photon energy. These slow electrons, which were also seen at photon energies below IE(He), are formed via an indirect mechanism involving substantial cooling of the photoelectron by the droplet atoms. Possible processes leading to this cooling include formation of an electron bubble, trapping of the electron in a surface-bound Rydberg state that undergoes vibrational autoionization, or a combination of the two. Evaporation of droplet atoms associated with cation core formation may also occur on a time scale similar to that of slow electron production.

Acknowledgment. D.M.N. thanks Roger Miller for many stimulating discussions about He droplets. The field is not the same without him. J.H.K. gratefully acknowledges the Korea Science and Engineering Foundation (KOSEF) for a postdoctoral fellowship. D.S.P. thanks Heather Whitley both for useful discussion and for altering the Universal Path Integral code to generate the nearest-neighbor distributions. This work was supported by the Director, Office of Science, Office of Basic Energy Sciences, Chemical Sciences Division of the U.S. Department of Energy under Contract No. DE-AC02-05CH11231.

References and Notes

(1) Northby, J. A. *J. Chem. Phys.* **2001**, *115*, 10065.
(2) Buchenau, H.; Toennies, J. P.; Northby, J. A. *J. Chem. Phys.* **1991**, *95*, 8134.
(3) Lewerenz, M.; Schilling, B.; Toennies, J. P. *J. Chem. Phys.* **1995**, *102*, 8191.
(4) Callicoatt, B. E.; Forde, K.; Jung, L. F.; Ruchti, T.; Janda, K. C. *J. Chem. Phys.* **1998**, *109*, 10195.
(5) Callicoatt, B. E.; Forde, K.; Ruchti, T.; Jung, L. L.; Janda, K. C.; Halberstadt, N. *J. Chem. Phys.* **1998**, *108*, 9371.
(6) Ruchti, T.; Forde, K.; Callicoatt, B. E.; Ludwigs, H.; Janda, K. C. *J. Chem. Phys.* **1998**, *109*, 10679.
(7) Ovchinnikov, M.; Grigorenko, B. L.; Janda, K. C.; Apkarian, V. A. *J. Chem. Phys.* **1998**, *102*, 9351.
(8) Ruchti, T.; Callicoatt, B. E.; Janda, K. C. *Phys. Chem. Chem. Phys.* **2000**, *2*, 4075.
(9) Fröchtenicht, R.; Henne, U.; Toennies, J. P.; Ding, A.; Fiebererdmann, M.; Drewello, T. *J. Chem. Phys.* **1996**, *104*, 2548.
(10) Peterka, D. S.; Kim, J. H.; Wang, C. C.; Neumark, D. M. *J. Phys. Chem. B* **2006**, *110*, 19945.
(11) Kim, J. H.; Peterka, D. S.; Wang, C. C.; Neumark, D. M. *J. Chem. Phys.* **2006**, *124*, 214301.
(12) Polyakova, E.; Stolyarov, D.; Wittig, C. *J. Chem. Phys.* **2006**, *124*, 214308.
(13) Peterka, D. S.; Lindinger, A.; Poisson, L.; Ahmed, M.; Neumark, D. M. *Phys. Rev. Lett.* **2003**, *91*, 043401.
(14) Radcliffe, P.; Przystawik, A.; Diederich, T.; Doppner, T.; Tiggesbaumker, J.; Meiwes-Broer, K. H. *Phys. Rev. Lett.* **2004**, *92*, 173403.
(15) Loginov, E.; Rossi, D.; Drabbels, M. *Phys. Rev. Lett.* **2005**, *95*, 163401.
(16) Heimann, P. A.; Koike, M.; Hsu, C. W.; Blank, D.; Yang, X. M.; Suits, A. G.; Lee, Y. T.; Evans, M.; Ng, C. Y.; Flaim, C.; Padmore, H. A. *Rev. Sci. Instrum.* **1997**, *68*, 1945.
(17) Buchenau, H.; Knuth, E. L.; Northby, J.; Toennies, J. P.; Winkler, C. *J. Chem. Phys.* **1990**, *92*, 6875.
(18) Harms, J.; Toennies, J. P.; Dalfovo, F. *Phys. Rev. B* **1998**, *58*, 3341.
(19) Knuth, E. L.; Schilling, B.; Toennies, J. P. *Rarefied Gas Dynamics, Proceedings of the International Symposium, 19th, Oxford, July 25−29, 1994*; Oxford University Press: Oxford, 1995.
(20) Toennies, J. P.; Vilesov, A. F. *Angew. Chem., Int. Ed.* **2004**, *43*, 2622.
(21) Wiley, W. C.; McLaren, I. H. *Rev. Sci. Instrum.* **1955**, *26*, 1150.
(22) Eppink, A. T. J. B.; Parker, D. H. *Rev. Sci. Instrum.* **1997**, *68*, 3477.
(23) Whitaker, B. J. Image Reconstruction: The Abel Transform. In *Imaging in Chemical Dynamics*; Suits, A., Continetti, R. E., Eds.; American Chemical Society: Washington, DC, 2001; Vol. 770; p 68.
(24) Garcia, G. A.; Nahon, L.; Powis, I. *Rev. Sci. Instrum.* **2004**, *75*, 4989.
(25) Kobayashi, N.; Kojima, T.; Kaneko, Y. *J. Phys. Soc. Jpn.* **1988**, *57*, 1528.
(26) Woolf, M. A.; Rayfield, G. W. *Phys. Rev. Lett.* **1965**, *15*, 235.
(27) Rosenblit, M.; Jortner, J. *Phys. Rev. Lett.* **1995**, *75*, 4079.
(28) Cooper, J.; Zare, R. N. *J. Chem. Phys.* **1968**, *48*, 942.
(29) Harms, J.; Toennies, J. P.; Knuth, E. L. *J. Chem. Phys.* **1997**, *106*, 3348.
(30) Jiang, T.; Northby, J. A. *Phys. Rev. Lett.* **1992**, *68*, 2620.
(31) Lewerenz, M.; Schilling, B.; Toennies, J. P. *Chem. Phys. Lett.* **1993**, *206*, 381.
(32) Henne, U.; Toennies, J. P. *J. Chem. Phys.* **1998**, *108*, 9327.
(33) Faubel, M. *Photoelectron Spectroscopy at Liquid Surfaces*; World Scientific: River Edge, NJ, 2000.
(34) Carnovale, F.; Peel, J. B.; Rothwell, R. G.; Valldorf, J.; Kuntz, P. J. *J. Chem. Phys.* **1989**, *90*, 1452.
(35) Jortner, J. *Z. Phys. D* **1992**, *24*, 247.
(36) Bader, J. S.; Cortis, C. M.; Berne, B. J. *J. Chem. Phys.* **1997**, *106*, 2372.
(37) Chin, S. A.; Krotscheck, E. *Phys. Rev. B* **1995**, *52*, 10405.
(38) Chase, C. E.; Maxwell, E.; Millett, W. E. *Physica* **1961**, *27*, 1129.
(39) Donnelly, R. J.; Barenghi, C. F. *J. Phys. Chem. Ref. Data* **1998**, *27*, 1217.
(40) Grandinetti, F. *Int. J. Mass. Spectrom.* **2004**, *237*, 243.
(41) Scifoni, E.; Gianturco, F. A. *Eur. Phys. J. D* **2002**, *21*, 323.
(42) Ganteför, G.; Broker, G.; Holubkrappe, E.; Ding, A. *J. Chem. Phys.* **1989**, *91*, 7972.
(43) Carnovale, F.; Peel, J. B.; Rothwell, R. G. *J. Chem. Phys.* **1991**, *95*, 1473.
(44) Tang, K. T.; Toennies, J. P.; Yiu, C. L. *Phys. Rev. Lett.* **1995**, *74*, 1546.
(45) Janzen, A. R.; Aziz, R. A. *J. Chem. Phys.* **1997**, *107*, 914.
(46) Ceperley, D. M. *Rev. Mod. Phys.* **1995**, *67*, 279.
(47) Whitley, H. Personal communication.

(48) Scifoni, E.; Dellepiane, G.; Gianturco, F. A. *Eur. Phys. J. D* **2004**, *30*, 353.
(49) Northby, J. A.; Sanders, T. M. *Phys. Rev. Lett.* **1967**, *18*, 1184.
(50) Hernande, J. P.; Silver, M. *Phys. Rev. A* **1970**, *2*, 1949.
(51) Grimes, C. C.; Adams, G. *Phys. Rev. B* **1992**, *45*, 2305.
(52) Fárník, M.; Toennies, J. P. *J. Chem. Phys.* **2003**, *118*, 4176.
(53) von Haeften, K.; Laarmann, T.; Wabnitz, H.; Möller, T. *J. Phys. B: At. Mol. Opt. Phys.* **2005**, *38*, S373.
(54) Benderskii, A. V.; Zadoyan, R.; Schwentner, N.; Apkarian, V. A. *J. Chem. Phys.* **1999**, *110*, 1542.
(55) Joppien, M.; Karnbach, R.; Möller, T. *Phys. Rev. Lett.* **1993**, *71*, 2654.
(56) Baym, G.; Barrera, R. G.; Pethick, C. J. *Phys. Rev. Lett.* **1969**, *22*, 20.
(57) Hori, H.; Ichikawa, O.; Wake, M.; Date, M. *J. Phys. Soc. Jpn.* **1973**, *35*, 1184.
(58) Jortner, J.; Kestner, N. R.; Rice, S. A.; Cohen, M. H. *J. Chem. Phys.* **1965**, *43*, 2614.
(59) Rosenblit, M.; Jortner, J. *J. Chem. Phys.* **2006**, *124*, 194505.
(60) Crandall, R. S.; Williams, R. *Phys. Rev. A* **1972**, *5*, 2183.
(61) Rosenblit, M.; Jortner, J. *J. Chem. Phys.* **1994**, *101*, 9982.
(62) Northby, J. A.; Kim, C. *Physica B* **1994**, *194*, 1229.
(63) Schoepe, W.; Probst, C. *Phys. Lett. A* **1970**, *A31*, 490.
(64) Ancilotto, F.; Toigo, F. *Phys. Rev. B* **1994**, *50*, 12820.
(65) Ancilotto, F.; Toigo, F. *Z. Phys. B* **1995**, *98*, 309.
(66) Fárník, M.; Samelin, B.; Toennies, J. P. *J. Chem. Phys.* **1999**, *110*, 9195.
(67) Rosenblit, M.; Jortner, J. *Phys. Rev. B* **1995**, *52*, 17461.
(68) Jortner, J.; Rosenblit, M. *Pol. J. Chem.* **1998**, *72*, 1447.
(69) Rosenblit, M.; Jortner, J. *J. Phys. Chem.* **1994**, *98*, 9365.
(70) Northby, J. A.; Kim, C.; Jiang, T. *Physica B* **1994**, *197*, 426.
(71) Fárník, M.; Henne, U.; Samelin, B.; Toennies, J. P. *Phys. Rev. Lett.* **1998**, *81*, 3892.
(72) Rosenblit, M.; Jortner, J. *J. Chem. Phys.* **2006**, *124*, 194506.
(73) Golov, A.; Sekatskii, S. *Z. Phys. D* **1993**, *27*, 349.
(74) Lewis, W. K.; Bemish, R. J.; Miller, R. E. *J. Chem. Phys.* **2005**, *123*, 141103.
(75) Lewis, W. K.; Applegate, B. E.; Sztáray, J.; Sztáray, B.; Baer, T.; Bemish, R. J.; Miller, R. E. *J. Am. Chem. Soc.* **2004**, *126*, 11283.
(76) Rosenblit, M.; Jortner, J. *J. Phys. Chem. A* **1997**, *101*, 751.
(77) Scifoni, E.; Bodo, E.; Dellepiane, G.; Gianturco, F. A. *Eur. Phys. J. D* **2004**, *30*, 363.
(78) Campbell, E. E. B.; Levine, R. D. *Annu. Rev. Phys. Chem.* **2000**, *51*, 65.
(79) Bordas, C.; Pinare, J. C.; Baguenard, B.; Broyer, M. *J. Phys. IV* **2000**, *10*, 55.
(80) Baguenard, B.; Pinare, J. C.; Bordas, C.; Broyer, M. *Phys. Rev. A* **2001**, *63*, 023204.